processes

MDPI

Article

Morphological Evolution of a Plastic Zone Surrounding a Circular Wellbore in Natural Gas Hydrate-Bearing Sediments

Shasha Li [1], Yuzhao Shi [2] and Wan Cheng [2,*]

[1] Artificial Intelligence School, Wuchang University of Technology, Wuhan 430223, China
[2] Faculty of Engineering, China University of Geosciences, Wuhan 430074, China
* Correspondence: chengwancup@163.com

Abstract

Wellbore instability poses a significant challenge to the safe and long-term production of natural gas hydrates (NGHs). Characterizing the geometry of the wellbore-adjacent plastic zone is critical for evaluating geomechanical risks during hydrate exploitation. In this paper, an elastic–plastic analytical model incorporating the Mohr–Coulomb failure criterion is developed to describe the stress distribution around the borehole under non-uniform in situ stress conditions. Particular attention is paid to the role of hydrate saturation, which is integrated into the constitutive framework to reflect the cementation effect of NGH-bearing sediments (GHBS). Analytical solutions for the stress fields in both the elastic and plastic regions are derived, which are accompanied by a computational scheme for determining the plastic zone radius. Using site-specific mechanical parameters from the Shenhu area in the South China Sea, a parametric analysis is conducted to quantify the influences of hydrate saturation, reservoir depressurization, and stress anisotropy on the evolution of the plastic zone shape. The results indicate that elevated hydrate saturation enhances the load-bearing capacity of the formation, whereas depressurization significantly expands the plastic region, leading to severe wellbore instability. These findings provide theoretical insights for optimizing drilling strategies in deep-water hydrate reservoirs.

Keywords: natural gas hydrate; wellbore stability; plastic zone; elastic zone; horizontal well

1. Introduction

Natural gas hydrate represents a vast reserve of clean energy characterized by its widespread occurrence and immense resource potential [1,2]. Consequently, numerous exploration and production trials have been conducted globally over the past few decades. However, wellbore instability remains a predominant geomechanical constraint impeding the safe and efficient development of NGH reservoirs [3,4]. In particular, the mechanical behavior of GHBS is highly sensitive to perturbations in the pressure, leading to complex borehole failure modes. Therefore, elucidating the mechanisms governing wellbore instability is a prerequisite for accurately predicting wellbore collapse and formulating effective mitigation strategies during drilling operations.

NGH predominantly comprises methane and water, which are stabilized under geo-environmental conditions of low temperature and high pressure. During drilling and production, the thermodynamic equilibrium near the wellbore is disturbed, rendering the hydrate phase highly susceptible to variations in temperature and pressure. Among various recovery strategies, depressurization has been widely validated as an effective and feasible method for NGH production [5–7]. However, this process induces NGH dissociation,

Check for updates

Academic Editor: Sai Liu

Received: 12 July 2026
Revised: 24 July 2026
Accepted: 26 July 2026
Published: 28 July 2026

Copyright: © 2026 by the authors. Licensee MDPI, Basel, Switzerland. This article is an open access article distributed under the terms and conditions of the Creative Commons Attribution (CC BY) license.

which degrades the cementation between hydrate crystals and sediment grains, thereby markedly reducing the strength and stiffness of GHBS. Experimental investigations by Liu et al. [8] further quantified this degradation, revealing that the cohesion and internal friction angle are strongly dependent on NGH saturation. Additionally, the Young's modulus exhibits a higher sensitivity to NGH saturation compared to the Poisson's ratio [9]. Given that the plastic deformation of the surrounding formation typically precedes macroscopic wellbore collapse, understanding the elastoplastic mechanical response of GHBS under varying saturation levels is imperative for maintaining borehole stability and even wellhead stability [10].

Extensive efforts have been devoted to developing wellbore stability models for NGH reservoirs under diverse physico-chemical conditions [11–13]. Early studies proposed a semi-analytical model utilizing the mechanical parameters of tetrahydrofuran hydrates to characterize borehole stability in synthetic hydrate formations. Subsequently, Freij-Ayoub et al. [14] advanced an analytical framework that integrated thermodynamic equilibrium, heat transfer, porous flow, and geomechanical deformation. Building on conventional wellbore stability theories, Ning et al. [15] established a fluid–solid coupling model to account for drilling fluid invasion. More recently, Sun et al. [16] developed a coupled thermo-hydro-mechanical (THM) framework to evaluate wellbore stability in GHBS, explicitly incorporating the effects of pore water salinity and drilling fluid infiltration. Concurrently, Cheng et al. [3] proposed a porothermoelastic model tailored for riserless drilling through GHBS, emphasizing temperature conduction and mud circulation along the entire wellbore. However, despite these advancements, the aforementioned models predominantly focus on the initiation of instability or the magnitude of pore pressure, often overlooking the evolution of the plastic zone induced by strength degradation (strain softening) and stress redistribution around the borehole. Consequently, the quantitative characterization of the elastoplastic deformation mechanism under the coupled effects of hydrate dissociation and non-uniform in situ stresses remains incomplete.

The quantification of the plastic zone radius around circular openings has been extensively studied using classical solutions, such as the modified Fenner's and Kastner's formulas [17]. Park et al. [18,19] further extended these analyses by deriving closed-form analytical solutions for elastoplastic-brittle rock masses conforming to the Mohr–Coulomb and Hoek–Brown failure criteria. Qian et al. [20] proposed a hypoplastic model for hydrate-bearing sands that integrates hydrate saturation and grain breakage. Guo et al. [4] presented an elastoplastic analytical solution for wellbore stability in GHBS, incorporating hydrate dissociation induced degradation and partial THM coupling. Li et al. [21] established a THM coupling model to investigate wellbore stability, incorporating the creep behavior of GHBS during extended drilling.

However, these foundational studies predominantly assume isotropic in situ stress conditions, resulting in a circular plastic zone geometry. In field scenarios involving deviated or horizontal wells, the far-field stress field is inherently anisotropic; consequently, the plastic region evolves into complex morphologies, including elliptical or butterfly-shaped configurations [22,23]. While these studies capture the geometric complexity induced by stress anisotropy, they largely neglect the concomitant degradation of mechanical strength. This oversight is critical for GHBS, where hydrate dissociation triggered by depressurization or thermal disturbance leads to significant cementation loss. Extensive experiments demonstrated that the cohesion and internal friction angle of GHBS exhibit a strong correlation with NGH saturation [8,9]. Therefore, any realistic stability analysis must account for the dynamic reduction in rock strength (i.e., strength softening) rather than treating mechanical parameters as constants. The mechanical behavior of HBS is governed by

hydrate cementation/filling, inducing overconsolidated soil characteristics, and further modulated by environmental conditions [24,25].

Motivated by these limitations, this paper develops an improved elastoplastic theoretical model for the stress field around boreholes in GHBS. Distinct from previous studies, the proposed model concurrently integrates three critical yet often isolated factors: (1) the strength softening induced by the reduction in hydrate saturation, (2) the depressurization effect during hydrate production, and (3) the non-uniform in situ stress field characteristic. By embedding the experimentally derived relationship between hydrate saturation and shear strength parameters into the Mohr–Coulomb failure criterion, closed-form analytical solutions for the stress distributions in both the elastic and plastic regions are derived. The model is capable of precisely characterizing the transition of the plastic zone morphology—from circular to elliptical and even butterfly-shaped configurations—under varying stress anisotropies and hydrate saturation levels. This paper provides a robust theoretical basis for predicting wellbore collapse and optimizing drilling strategies in deep-water hydrate reservoirs.

2. Model Establishment

2.1. Problem Description

Marine NGH deposits typically reside 200~400 m below the seafloor (e.g., the Shenhu area of the South China Sea), where the effective stress acting on the GHBS skeleton is on the order of several MPa. Triaxial tests on marine GHBS cores reveal a propensity for plastic deformation under deviatoric stress [26]. Notably, Xu et al. [27] demonstrated that hydrates significantly enhance the strength and stiffness of GHBS under low effective confining pressures (ECP, Figure 1). Under these conditions, the stress–strain response exhibits nearly linear elasticity prior to peak strength, which is followed by a distinct plateau indicative of approximately ideal elastic–plastic behavior. Consistent with these findings, Zhang et al. [28] reported similar ideal elastic–plastic characteristics across a series of tests involving varying ECPs (Figure 2).

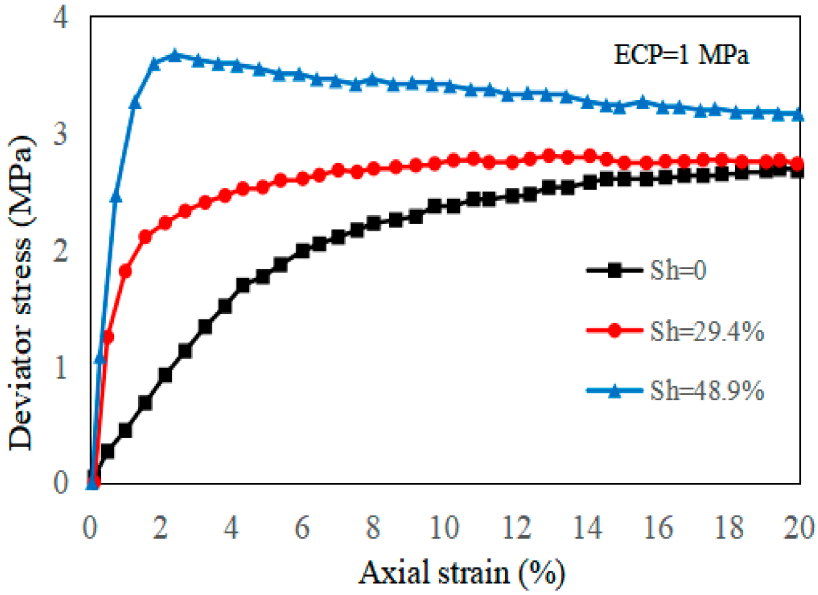


Figure 1. Deviator stress vs. axial strain under different NGH saturation levels [27].

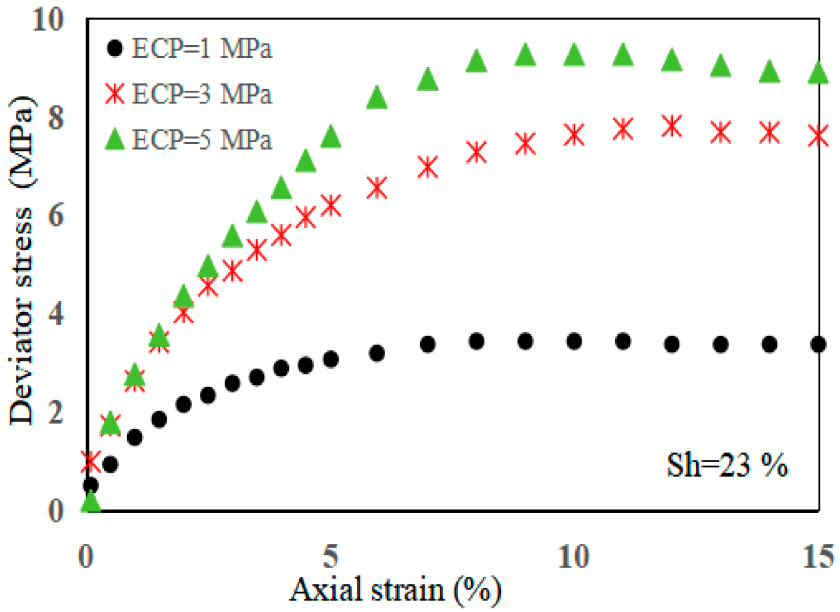


Figure 2. Deviator stress vs. axial strain under different ECPs [28].

Extensive experimental studies [8,9] have established empirical correlations between the shear strength parameters (friction angle and cohesion), Young's modulus of GHBS, and NGH saturation, which are expressed as

$$\varphi(S_h) = \begin{cases} 35S_h + 35.9 & S_h \le 23.86\% \\ -38S_h + 53.2 & S_h > 23.86\% \end{cases} \quad (1)$$

$$\mathrm{c}(S_h) = c_0(1 + 3S_h) \qquad 0 \le S_h \le 50\% \quad (2)$$

$$E(S_h) = E_0(1 + 13.25S_h) \quad (3)$$

where S_h is the saturation of NGH; c_0 is the cohesion of GHBS when S_h = 0, MPa; E_0 is the Young's modulus of GHBS when S_h = 0, MPa; E is the Young's modulus of GHBS; c is the cohesion of GHBS, MPa; and φ is the internal friction angle, °.

2.2. Basic Assumptions

Some assumptions should be made to drive the stress field surrounding the borehole in GHBS.

(1) The GHBS is assumed as an isotropic continuum. The plane perpendicular to the borehole axis satisfies the plane strain condition.
(2) The horizontal well suffers non-uniform far-field stresses and uniform fluid pressure inside the wellbore (Figure 3). The borehole radius is R_0 and the outer radius of the plastic zone is R_p.
(3) The compressive stress and the displacement toward the borehole center are positive.
(4) The deformation is simplified as elastic–plastic (Figure 4).
(5) Poroelasticity is ignored since the permeability of GHBS is extremely low. Under short-term drilling operations, the assumption of a quasi-static pore pressure (determined by the depressurization schedule) is acceptable, and the elastic–plastic boundary is mainly controlled by the updated effective stress rather than by transient diffusion. Under long-term production, ignoring hydro-mechanical coupling would underestimate the rate of pore-pressure dissipation and thus overestimate the effective stress increase, potentially predicting a larger plastic zone than a fully coupled model would.

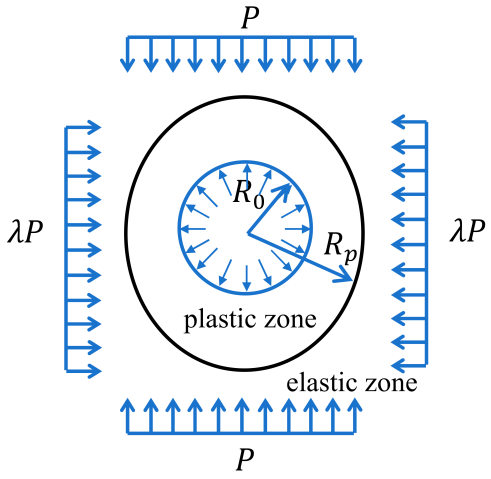


Figure 3. Plastic and elastic zones around a wellbore. P is the confining stress and λ is a proportionality constant.

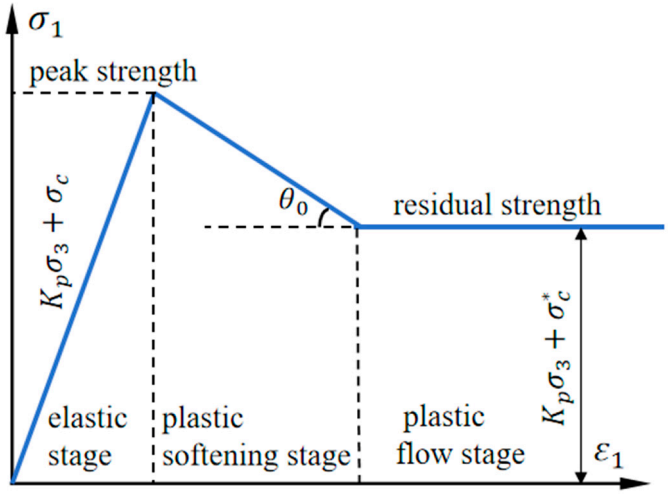


Figure 4. Typical stress–strain curve (Adapted from [21]) © 2020 by the authors. Licensee MDPI, Basel, Switzerland. This article is an open access article distributed under the terms and conditions of the Creative Commons Attribution (CC BY) license (http://creativecommons.org/licenses/by/4.0/, accessed on 25 July 2026).

The strain-softening degree of the surrounding rock after reaching the peak strength is labeled as θ_0. When $\theta_0 = 0°$, it becomes the ideal elastic–plastic model. When $\theta_0 = 90°$, it becomes an elastic–brittle–plastic model. Figure 4 shows that the stress–strain curve can be divided into three stages: elastic deformation stage, plastic softening stage and plastic flow stage (Figure 4).

2.3. Fundamental Equations

(1) Elastic deformation stage

It is assumed the surrounding rock of the borehole satisfies the Mohr–Coulomb criterion when yielding occurs.

$$\sigma_1 = K_p\sigma_3 + \sigma_c \tag{4a}$$

$$\sigma_c = \frac{2c \cdot cos\varphi}{1 - sin\varphi} \tag{4b}$$

$$K_p = \frac{1 + sin\varphi}{1 - sin\varphi} \tag{4c}$$

where σ_1 and σ_3 are the maximum and minimum principal stresses, respectively. σ_c is the uniaxial compressive strength, MPa. K_p is the confining stress coefficient.

(2) Plastic flow stage

$$\sigma_1 = K_p \sigma_3 + \sigma_c^* \tag{5}$$

where σ_c^* is the residual strength in the plastic zone under uniaxial compression.

3. Analytical Stresses of the Elastic-Plastic Zone

3.1. Elastic Zone

The stress field of the borehole surrounding mass under a non-uniform stress field is the superposition of an internal compressive stress field by the fluid pressure and biaxial compressive stress field by the far field (Figure 5).

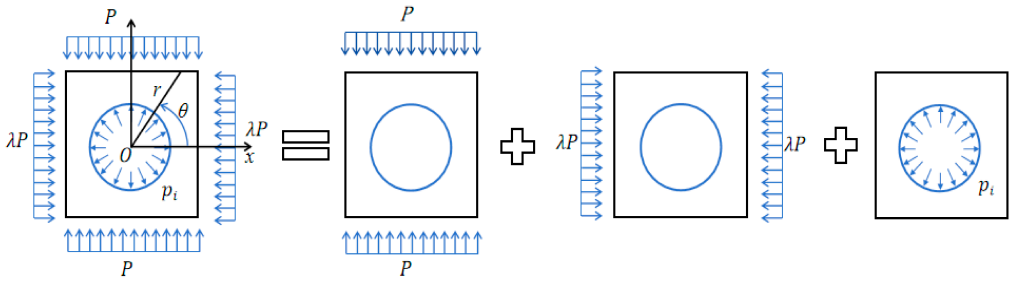


Figure 5. Stress field decomposition.

The boundary conditions are

$$\sigma_r|_{r\to\infty} = P/2[1 + \lambda + (\lambda - 1)cos2\theta] \tag{6}$$

$$\sigma_\theta|_{r\to\infty} = P/2[1 + \lambda - (\lambda - 1)cos2\theta] \tag{7}$$

$$\sigma_\theta|_{r=R_p} = K_p\sigma_r + \sigma_c \tag{8}$$

where θ is the anticlockwise angle from the x-axis, rad; σ_r is the radial stress, MPa; and σ_θ is the circumferential stress, MPa. $\tau_{r\theta}$ is the shear stress, MPa.

The following solutions can be obtained in the elastic zones,

$$\sigma_r = \frac{P(1+\lambda)}{2} - \frac{\sigma_c + P/2(K_p-1)(1+\lambda)}{K_p+1}\left(\frac{R_p}{r}\right)^2 - \left[\frac{P(1-\lambda)}{2} + \frac{2P(K_p+1)(1-\lambda)}{1-K_p}\left(\frac{R_p}{r}\right)^2 + \frac{P(3K_p+1)(\lambda-1)}{2(1-K_p)}\left(\frac{R_p}{r}\right)^4\right]cos2\theta \tag{9}$$

$$\sigma_\theta = \frac{P(1+\lambda)}{2} + \frac{\sigma_c + P/2(K_p-1)(1+\lambda)}{K_p+1}\left(\frac{R_p}{r}\right)^2 + \left[\frac{P(1-\lambda)}{2} + \frac{P(3K_p+1)(\lambda-1)}{2(1-K_p)}\left(\frac{R_p}{r}\right)^4\right]cos2\theta \tag{10}$$

$$\tau_{r\theta} = \left[\frac{P(1-\lambda)}{2} - \frac{P(K_p-1)(1+\lambda)}{K_p+1}\left(\frac{R_p}{r}\right)^2 - \frac{P(3K_p+1)(\lambda-1)}{2(1-K_p)}\left(\frac{R_p}{r}\right)^4\right]sin2\theta \tag{11}$$

At the junction of the elastic and plastic zones,

$$\sigma_r|_{r=R_p} = \frac{P(1+\lambda)-\sigma_c}{K_p+1} + \frac{2P(1-\lambda)}{K_p-1}cos2\theta \tag{12}$$

$$\sigma_\theta|_{r=R_p} = \frac{P(1+\lambda)K_p+\sigma_c}{K_p+1} + \frac{2P(1-\lambda)K_p}{K_p-1}cos2\theta \tag{13}$$

$$\tau_{r\theta}|_{r=R_p} = 0 \tag{14}$$

Equations (12)–(14) depend on the values of P, c, and φ, and they are independent of p_i.

3.2. Plastic Zone

The equilibrium differential equation in the plastic zone is

$$\frac{\partial \sigma_r}{\partial r} + \frac{1 - K_p}{r}\sigma_r = \frac{\sigma_c}{r} \tag{15}$$

By using the boundary condition expressed by Equations (12)–(14), we can obtain

$$\sigma_r = \frac{\sigma_c}{1 - K_p} + [\frac{P(1+\lambda) - \sigma_c}{K_p + 1} + \frac{\sigma_c}{K_p - 1}](\frac{R_p}{r})^{1-K_p} + \frac{2P(1-\lambda)}{1 - K_p}(\frac{R_p}{r})^{1-K_p} cos2\theta \tag{16}$$

$$\sigma_\theta = \frac{\sigma_c}{1 - K_p} + K_p[\frac{P(1+\lambda) - \sigma_c}{K_p + 1} + \frac{\sigma_c}{K_p - 1}](\frac{R_p}{r})^{1-K_p} + \frac{2PK_p(1-\lambda)}{1 - K_p}(\frac{R_p}{r})^{1-K_p} cos2\theta \tag{17}$$

The internal stress condition is

$$\sigma_r|_{r=R_0} = p_i \tag{18}$$

By using the internal stress condition, we can obtain

$$\frac{\sigma_c}{1 - K_p} + [\frac{P(1+\lambda) - \sigma_c}{K_p + 1} + \frac{\sigma_c}{K_p - 1}](\frac{R_p}{r})^{1-K_p} + \frac{2P(1-\lambda)}{1 - K_p}(\frac{R_p}{r})^{1-K_p} cos2\theta - p_i = 0 \tag{19}$$

Equation (19) is solved to obtain the plastic zone R_p.

4. Case Study of NGH Reservoirs in the China Shenhu Area

4.1. Fundamental Parameters of the Shenhu NGH Reservoir

The parameters of the NGH reservoirs in the China Shenhu area are given in Table 1. To date, studies on the mechanical stability of clayey silt and silty clay NGH reservoirs in the China Shenhu area are rare [11]. Based on previous drilling results from the China Shenhu area, we study the effects of NGH saturation and depressurization on elastic and plastic zones in a non-uniform in situ stress field.

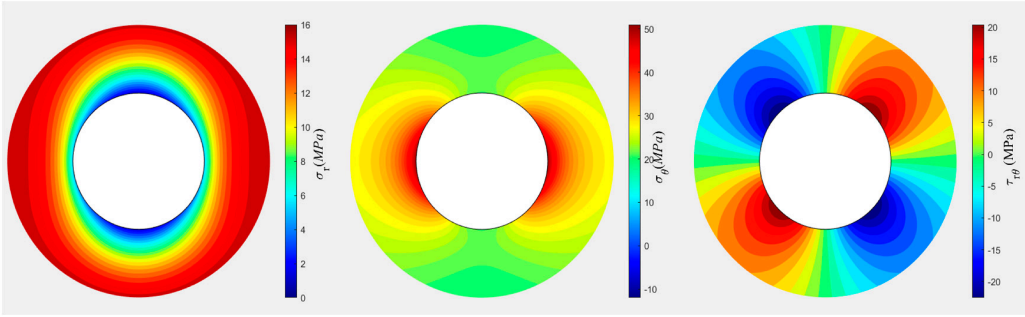
Table 1. Fundamental parameters of the Shenhu NGH reservoir (GMGS3-W19).

Parameter	Value
Cohesion	$c = c_0(1 + 3S_h)$, c_0 = 0.5 MPa
Friction angle	30°
Poisson's ratio	0.15
Vertical in situ stress	16.438 MPa
Sea depth	1273.9 m
Overlying layer thickness	135 m
NGH layer thickness	35 m
Underlying strata thickness	94 m
Initial NGH saturation	0.45
Softening degree of GHBS	0°

4.2. Stress Distribution in the Surrounding Rock Mass

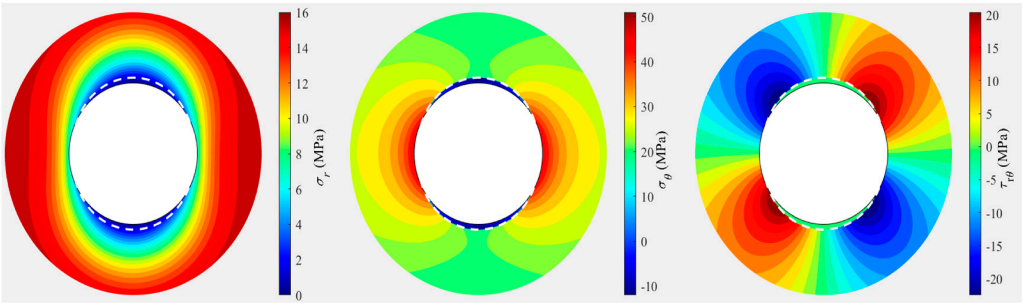
Based on the parameters of NGH reservoirs in the China Shenhu area, the effects of plastic deformation on the stress field cannot be ignored by a comparative analysis of the wellbore stress field with (Figure 6) and without (Figure 7) considering plastic deformation. The white dotted lines in Figure 7 indicate the boundary of the plastic zone. The radial stress increases in an elliptical shape toward the outside of the well, and the circumferential stress in the transverse axis decreases in an arc-like shape toward the outside of the well

(Figure 6). Relative to those in the scenarios without plastic deformation, the stress in the radial stress field is lower in the region with stress values less than 4 MPa (depicted in blue). In addition, the area with a stress value of approximately 15 MPa in the longitudinal axis direction is reduced. In the circumferential stress field, tensile stresses begin to appear around the wellbore wall with the maximum tensile stress reaching 11.15 MPa.



(**a**) Radial stress field (**b**) Radial stress field (**c**) Shear stress field

Figure 6. Stress field without plastic deformation. P = 16.438 MPa, λ = 1.4.



(**a**) Radial stress field (**b**) Radial stress field (**c**) Shear stress field

Figure 7. Stress field with plastic deformation. P = 16.438 MPa, λ = 1.4.

4.3. Effects of Saturation on the Size and Shape of the Plastic Zone

The shape of the plastic zone is affected by the NGH saturation, as shown in Figure 8. Assume that the ratio of the pressure reduction amount to the initial pore pressure is γ, the NGH saturation is S_h, and the lateral stress coefficient is λ. The lateral stress coefficient is setto1.4. When the ratio of the pressure reduction amount to the initial pore pressure is constant, the size of the plastic zone decreases with increasing NGH saturation. With an increase in the ratio of the pressure reduction to the initial pore pressure, the boundaries of the plastic zone in the transverse direction gradually concentrate. However, the boundaries of the plastic zone in the longitudinal direction are gradually dispersed. When $r/R_0 < 1$, no plastic zone appears.

4.4. Effects of Depressurization on the Size and Shape of the Plastic Zone

As depicted in Figure 9, the shape of the plastic zone is affected by depressurization. λ is set to 1.4. When the NGH saturation is constant, the size of the plastic zone increases with an increase in the ratio of the pressure reduction to the initial pore pressure. As the NGH saturation increases, the boundary shape of the plastic zone changes, which is similar to the process of two bubbles gradually merging. When $r/R_0 < 1$, no plastic zone appears.

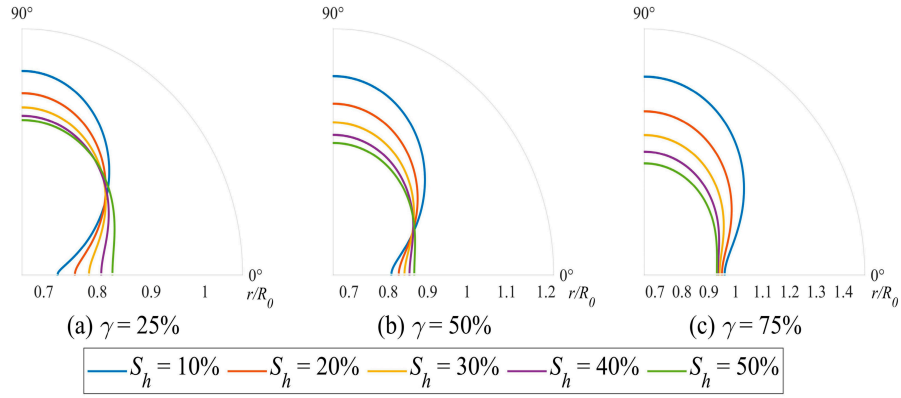


Figure 8. Boundaries of the plastic zone under varying NGH saturation.

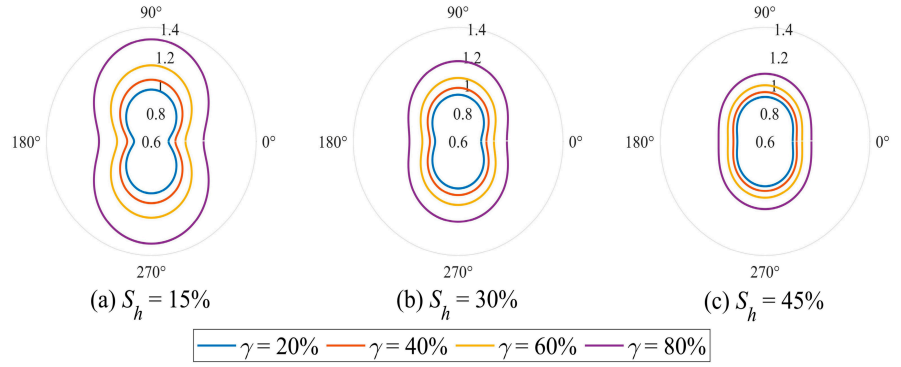


Figure 9. Boundaries of the plastic zone under varying ratios of the pressure reduction to the initial pore pressure.

4.5. Effects of the Lateral Stress Coefficient on the Size and Shape of the Plastic Zone

The NGH saturation is set to 50%, the ratio of the pressure reduction amount to the initial pore pressure is set to 0.6, and the lateral pressure coefficient is set to 1.0, 1.1, 1.2, 1.3 or 1.4, respectively. The plastic zone radii under different lateral stress coefficients are presented in Figure 10. The plastic zone around the wellbore exhibits a circular shape under a uniform in situ stress. As the lateral stress coefficient increases, the plastic zone becomes irregular, such as elliptical or butterfly shaped. Similar behavior is observed when the NGH saturation is set to different values.

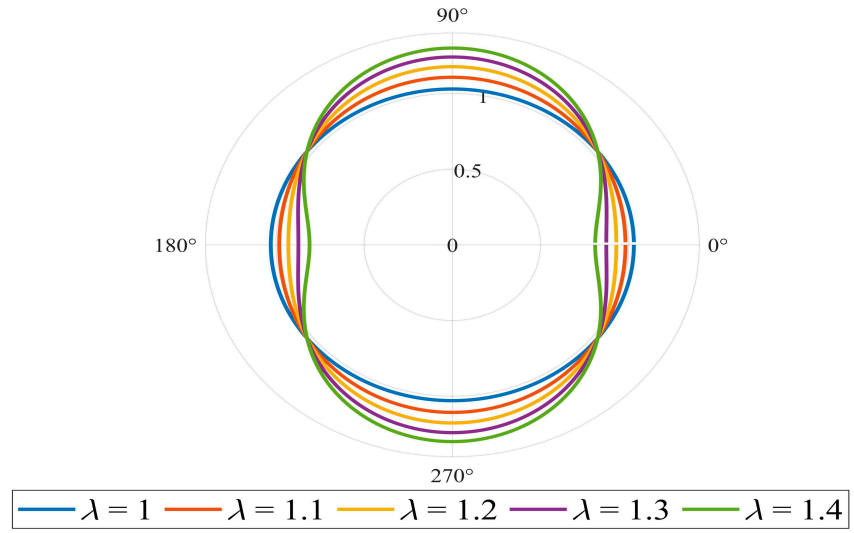


Figure 10. Boundaries of the plastic zone under varying lateral stress coefficients.

4.6. Effects of Depressurization and NGH Saturation on the Plastic Zone Area

Equation (19) can be solved to determine the radius of the plastic zone. The area of the plastic zone is recorded as *S*. Different plastic zone areas are obtained by varying the ratio of the pressure reduction amount to the initial pore pressure and varying the NGH saturation (Figure 11). When the area of the plastic zone is 0, no plastic zone is formed under the corresponding conditions of a specific ratio of the pressure reduction amount to the initial pore pressure and a specific NHG saturation. As shown in Figure 8, there is no plastic zone when the proportion of the pressure reduction amount to the initial pore pressure is less than 55%.

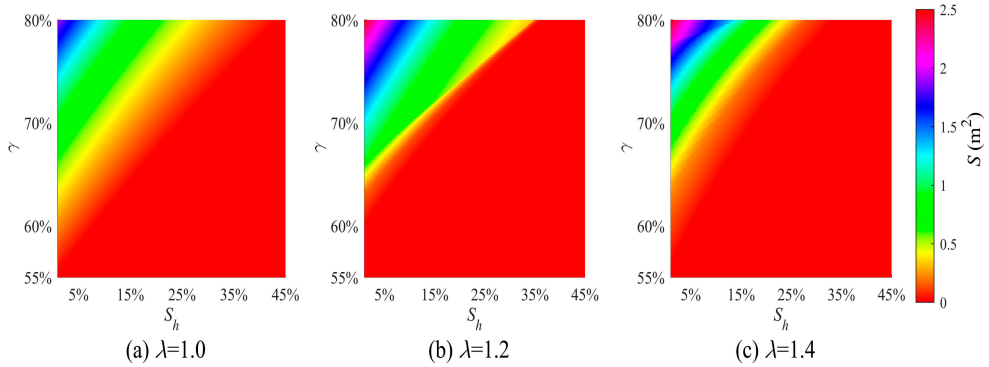


Figure 11. Plastic zone area under varying NGH saturation and ratios of the pressure reduction amount to the initial pore pressure.

As shown in Table 2, the absolute value of the plastic zone area change rate caused by the same pressure reduction decreases as the NGH saturation increases, and the corresponding plastic zone boundary line is shown in Figure 8. A comparative analysis of the three sub-figures under different lateral stress coefficients in Figure 10 indicates that there is no significant correlation between the area of the plastic zone and the lateral stress coefficient.

Table 2. Rate of change in the plastic zone area.

S_h	S (m^2)				[γ (40%) − γ (20%)]/ γ (20%)	[γ (60%) − γ (40%)]/ γ (40%)	[γ (80%) − γ (60%)]/ γ (60%)
	γ (20%)	γ (40%)	γ (60%)	γ (80%)			
15%	2.339	2.684	3.239	4.360	14.76%	20.67%	34.60%
30%	2.328	2.574	2.950	3.655	10.54%	14.61%	23.91%
45%	2.365	2.542	2.804	3.271	7.49%	10.32%	16.66%

5. Discussion

Beyond theoretical interest, our proposed model yields direct engineering implications for drilling operations in GHBS.

(1) The quantitative relationship between hydrate saturation and the plastic zone radius provides a basis for real-time mud weight optimization. As hydrate saturation decreases due to depressurization, the allowable mud weight window narrows significantly; therefore, maintaining a mud density slightly above the critical collapse pressure can effectively restrain the expansion of the plastic zone.

(2) Under non-uniform in situ stresses, the asymmetric morphology of the plastic zone (elliptical to butterfly-shaped) suggests that wellbore collapse is most likely to initiate at the azimuth of the minimum horizontal principal stress. Adjusting the well trajectory to avoid prolonged exposure of the weakest azimuth can mitigate localized shear failure.

(3) The results highlight that premature depressurization prior to casing setting dramatically increases the risk of wellbore instability; hence, a controlled depressurization schedule synchronized with casing programs is recommended to preserve the cementation effect of hydrates. These insights offer practical guidance for mitigating wellbore instability during the exploration and production of NGH.

6. Conclusions

(1) A theoretical model for the elastic–plastic stress field around a wellbore under non-uniform in situ stress is established along with a calculation method for the plastic zone area. Comparative analysis reveals that plastic deformation exerts a significant influence on the stress distribution, which cannot be neglected in stress field evaluations.

(2) Stress at the elastic–plastic interface is governed by the in situ stress, cohesion, and internal friction angle, but it remains independent of the wellbore internal pressure. Conversely, internal pressure serves as a primary control on the plastic zone geometry; variations in pressure directly induce the expansion or contraction of the yielded region.

(3) At a constant ratio of pressure drawdown to initial pore pressure, the plastic zone area diminishes with increasing NGH saturation. Concurrently, the plastic boundary tends to concentrate transversely while dispersing longitudinally. These results indicate that the presence of NGH effectively restrains plastic deformation in the surrounding sediments.

(4) At constant NGH saturation, both the plastic zone area and its boundary complexity increase with higher pressure drawdown and initial pore pressure. Notably, the plastic boundary evolves as adjacent lobes progressively coalesce. This suggests that enhanced depressurization creates more favorable conditions for plastic zone development.

(5) Under uniform in situ stress, the plastic zone adopts a circular shape. As the lateral stress coefficient increases, the zone transitions to elliptical or butterfly-shaped configurations. However, the total area of the plastic zone exhibits no significant correlation with the lateral stress coefficient.

(6) The proposed model offers practical guidance for field operations. The derived dependence of the plastic zone radius on NGH saturation allows for an optimization of drilling mud weights to counteract strength degradation. Furthermore, recognizing that the plastic zone evolves asymmetrically under stress anisotropy, targeting well trajectories away from the minimum horizontal stress azimuth and avoiding premature depressurization are recommended to prevent wellbore collapse.

Author Contributions: Conceptualization, S.L.; Methodology, Y.S.; Software, S.L.; Writing—original draft, S.L. and W.C.; Writing—review and editing, Y.S. and W.C.; Supervision, W.C. All authors have read and agreed to the published version of the manuscript.

Funding: This research was supported by the National Natural Science Foundation of China (No. 52074250).

Data Availability Statement: The original contributions presented in this paper are included in the article. Further inquiries can be directed to the corresponding author.

Conflicts of Interest: The authors declare no conflicts of interest.

Nomenclature

S_h	saturation of NGH, dimensionless
c_0	cohesion of GHBS when S_h = 0, MPa
c	cohesion of GHBS, MPa
E_0	the Young's modulus of GHBS when S_h = 0, MPa
E	the Young's modulus of GHBS, MPa
φ	internal friction angle, °
R_0	borehole radius, m
R_p	radius of plastic zone, m
P	confining stress, MPa
λ	proportionality constant, dimensionless
K_p	confining stress coefficient.
σ_1 and σ_3	the maximum and minimum principal stresses respectively, MPa
θ_0	strain softening degree, rad
σ_c	uniaxial compressive strength, MPa
σ_c^*	residual strength in the plastic zone under uniaxial compression, MPa
θ	anticlockwise angle from the x-axis, rad
σ_r	radial stress, MPa
σ_θ	circumferential stress, MPa.
$\tau_{r\theta}$	shear stress, MPa
p_i	internal pressure acting on the wellbore wall, MPa
γ	represents the ratio of the pressure reduction amount to the initial pore pressure, dimensionless

References

1. Chong, Z.R.; Yang, S.H.B.; Babu, P.; Linga, P.; Li, X. Review of natural gas hydrates as an energy resource: Prospects and challenges. *Appl. Energy* **2016**, *162*, 1633–1652. [CrossRef]
2. Yu, J.; Zhao, J.; Liang, W. Multiscale modeling of coupled thermo-hydro-mechanicalchemical behavior in hydrate-bearing sediment. *J. Mech. Phys. Solids* **2026**, *210*, 106512. [CrossRef]
3. Cheng, W.; Ning, F.; Sun, J.; Liu, Z.; Jiang, G.; Li, X. A porothermoelastic wellbore stability model for riserless drilling through gas hydrate-bearing sediments in the Shenhu area of the South China Sea. *J. Nat. Gas Sci. Eng.* **2019**, *72*, 103036. [CrossRef]
4. Guo, Z.; Wang, H.; Jiang, M. Elastoplastic analytical investigation of wellbore stability for drilling in methane hydrate-bearing sediments. *J. Nat. Gas Sci. Eng.* **2020**, *79*, 103344. [CrossRef]
5. Sang, S.; Kong, L.; Zhao, Y.; Liu, J.; Hua, L. Mechanical characterization of hydrate-bearing clayey-silty sediments with layered sediment distribution: Effects of hydrate saturation and effective confining pressure. *Ocean Eng.* **2025**, *326*, 120879. [CrossRef]
6. Uddin, M.; Wright, F.; Dallimore, S.; Coombe, D. Gas hydrate dissociations in Mallik hydrate bearing zones A, B, and C by depressurization: Effect of salinity and hydration number in hydrate dissociation. *J. Nat. Gas Sci. Eng.* **2014**, *21*, 40–63. [CrossRef]
7. Yamamoto, K.; Terao, Y.; Fujii, T.; Ikawa, T.; Seki, M.; Matsuzawa, M.; Kanno, T. Operational overview of the first offshore production test of methane hydrates in the Eastern Nankai Trough. In Proceedings of the Offshore Technology Conference, Houston, TX, USA, 5–8 May 2014.
8. Liu, Z.; Wei, H.; Peng, L.; Wei, C.; Ning, F. An easy and efficient way to evaluate mechanical properties of gas hydrate-bearing sediments: The direct shear test. *J. Pet. Sci. Eng.* **2017**, *149*, 56–64. [CrossRef]
9. Li, Q.; Li, Q.; Wu, J.; Li, X.; Li, H.; Cheng, Y. Wellhead stability during development process of hydrate reservoir in the northern south China sea: Evolution and mechanism. *Processes* **2025**, *13*, 40. [CrossRef]
10. Cheng, Y.; Xue, M.; Shi, J.; Li, Y.; Yan, C.; Han, Z.; Yang, J. Numerical simulating the influences of hydrate decomposition on wellhead stability. *Processes* **2023**, *11*, 1586. [CrossRef]
11. Sun, J.; Zhang, L.; Ning, F.; Lei, H.; Liu, T.; Hu, G.; Lu, H.; Lu, J.; Liu, C.; Jiang, G.; et al. Production potential and stability of hydrate-bearing sediments at the site GMGS3-W19 in the South China Sea: A preliminary feasibility study. *Mar. Pet. Geol.* **2017**, *86*, 447–473. [CrossRef]
12. Tan, C.; Yang, J.; Clennell, M.; Tohidi, B.; Freij-Ayoub, R. Mechanical and petrophysical characterisation and wellbore stability management in gas hydrate-bearing sediments. In Proceedings of the 40th U.S. Symposium on Rock Mechanics (USRMS), Anchorage, AK, USA, 25–29 June 2005.
13. Cheng, W.; Lu, C.; Ning, F.; Jia, M. A coupled thermal-hydraulic-mechanical model for the kinetic dissociation of methane hydrate in a depressurizing well. *J. Pet. Sci. Eng.* **2021**, *207*, 109021. [CrossRef]

14. Freij-Ayoub, R.; Tan, C.; Clennell, B.; Tohidi, B.; Yang, J. A wellbore stability model for hydrate bearing sediments. *J. Pet. Sci. Eng.* **2007**, *57*, 209–220. [CrossRef]
15. Ning, F.; Jiang, G.; Zhang, L.; Wu, X.; Dou, B.; Tu, Y. Analysis of key factors affecting wellbore stability in gas hydrate formations. *Pet. Drill. Tech.* **2008**, *36*, 59–61.
16. Sun, J.; Ning, F.; Lei, H.; Gai, X.; Sanchez, M.; Lu, J.; Li, Y.; Liu, L.; Liu, C.; Wu, N.; et al. Wellbore stability analysis during drilling through marine gas hydrate-bearing sediments in Shenhu area: A case study. *J. Pet. Sci. Eng.* **2018**, *170*, 345–367. [CrossRef]
17. Kastner, H. *Statik des Tunnel- und Stollenbaues*; Springer: Berlin/Heidelberg, Germany, 1971.
18. Park, K.-H.; Kim, Y.-J. Analytical solution for a circular opening in an elastic-brittle-plastic rock. *Int. J. Rock Mech. Min. Sci.* **2006**, *43*, 616–622. [CrossRef]
19. Park, K.-H.; Tontavanich, B.; Lee, J.-G. A simple procedure for ground response curve of circular tunnel in elastic-strain softening rock masses. *Tunn. Undergr. Space Technol.* **2008**, *23*, 151–159. [CrossRef]
20. Qian, H.; Wu, W.; Xu, C.; Du, X. A hypoplastic model for hydrate-bearing sand considering hydrate saturation and grain breakage. *Int. J. Numer. Anal. Methods Geomech.* **2023**, *47*, 3044–3064. [CrossRef]
21. Li, Y.; Cheng, Y.; Yan, C.; Wang, Z.; Song, L. Effects of creep characteristics of natural gas hydrate-bearing sediments on wellbore stability. *Pet. Sci.* **2022**, *19*, 220–233. [CrossRef]
22. Guo, X.; Zhao, Z.; Gao, X.; Wu, X.; Ma, N. Analytical solutions for characteristic radii of circular roadway surrounding rock plastic zone and their application. *Int. J. Min. Sci. Technol.* **2019**, *29*, 263–272. [CrossRef]
23. Shang, X.; Zhang, Z. Elastic-plastic-damaged zones around a deep circular wellbore under non-uniform loading. *Symmetry* **2020**, *12*, 323. [CrossRef]
24. Zhao, Y.; Liu, J.; Hua, L.; Kong, L.; Sang, S.; Yuan, Q. Mechanical characteristics of overconsolidated hydrate-bearing clayey-silty sediments with various confining pressures. *Acta Geotech.* **2023**, *18*, 3505–3527. [CrossRef]
25. Wang, L.; Liu, Z.; Yan, X.; Wu, Z.; Liu, Z.; Ma, S.; Li, Y. Stress-strain and creep behaviors of marine overconsolidated hydrate-bearing sediments. *Geoenergy Sci. Eng.* **2025**, *254*, 214036. [CrossRef]
26. Yoneda, J.; Masui, A.; Konno, Y.; Jin, Y.; Egawa, K.; Kida, M.; Ito, T.; Nagao, J.; Tenma, N. Mechanical properties of hydrate-bearing turbidite reservoir in the first gas production test site of the Eastern Nankai Trough. *Mar. Pet. Geol.* **2015**, *66*, 471–486. [CrossRef]
27. Xu, J.; Xu, C.; Huang, L.; Hyodo, M. Strength estimation and stress-dilatancy characteristics of natural gas hydrate-bearing sediments under high effective confining pressure. *Acta Geotech.* **2023**, *18*, 811–827.
28. Zhang, X.; Lin, J.; Lu, X.; Liu, L.; Liu, C.; Li, M.; Su, Y. A hypoplastic model for gas hydrate-bearing sandy sediments. *Int. J. Numer. Anal. Methods Geomech.* **2018**, *42*, 931–942. [CrossRef]

Disclaimer/Publisher's Note: The statements, opinions and data contained in all publications are solely those of the individual author(s) and contributor(s) and not of MDPI and/or the editor(s). MDPI and/or the editor(s) disclaim responsibility for any injury to people or property resulting from any ideas, methods, instructions or products referred to in the content.